Quantitative evaluation of 3D land acquisition geometries with arrays and single sensors: Closing the loop between acquisition and processing

Andrey Bakulin[1] and Ilya Silvestrov[1]

https://doi.org/10.1190/tle42050310.1

Abstract

The growing popularity of land nodes demands careful survey design practices to smoothly supersede cabled seismic acquisition with geophone arrays. Unfortunately, trace density is often used as a catchall proxy to describe survey quality, which is a gross oversimplification. We describe comprehensive and quantitative workflows focusing on final image quality for evaluating existing or new 3D land acquisition geometries with arrays and single sensors. They streamline the design process, remove human bias, and close the loop between acquisition and processing. A central element is a data-driven approach for deriving absolute signal-to-noise ratio (S/N) directly from the data. The resulting S/N volumes can be analyzed as cubes or slices or distilled to statistical quantities. We apply new workflows to three typical use cases from 3D land seismic data. First, we quantitatively contrast different 3D data sets acquired with various field acquisition geometries and understand which acquisition parameters are likely responsible for S/N differences. Second, we perform a realistic numerical feasibility study evaluating multiple 3D acquisition geometries with arrays and single sensors and assess their expected performance on a complex SEG Advanced Modeling Arid data set representative of the desert environment. For feasibility studies, complete automation can be achieved by applying migration in lieu of processing and data-driven S/N as evaluation steps. Finally, we show how to predict absolute S/N outcomes of new 3D acquisitions based on the existing legacy data with different acquisition geometry. We demonstrate the excellent predictive power of the analytical signal-strength estimate formula for both field and synthetic elastic data sets. Translating survey design into commonly spoken "image S/N language" improves communication between geoscientists and enables more effective decision-making.

Introduction

Seismic acquisition represents the largest portion of geophysical expenditures. Consequently, much effort goes into tinkering with the seismic acquisition. Survey design is a critical area of geophysical engineering. While significant experience has been accumulated (Vermeer, 2012), many parts remain qualitative. A survey design exercise conducted by the leading industry practitioners highlighted the diversity and the lack of quantitative metrics in many steps (Galbraith, 2000; Hornman and Vermeer, 2000a, 2000b; Lansley, 2000; Meunier and Gillot, 2000; Monk and Yates, 2000; Musser, 2000). In concluding remarks, Hornman and Vermeer (2000b) state, "The purpose of this review is not to present a verdict on their relative quality. The reader must make that judgment for himself." This makes acquisition design look more like art than science. It also puts interpreters and geoscientists in difficult positions when asked to contribute to selecting the best survey design. In an era when anything and everything is constantly evaluated with data-driven metrics, we believe it is time to upgrade survey design to a more quantitative engineering process that could improve geophysical engagement with other geoscientists consuming seismic imaging.

One analytic survey design approach from the aforementioned exercise by Meunier and Gillot (2000) stood out with its simplicity and completeness. It absorbed most of the acquisition parameters into a single formula expressing the signal-strength estimate (SSE) of the final image. The SSE formula is based on the simple assumption of any noise being suppressed according to the square-root law. However, these assumptions remain unverified for complex organized noise, as in land acquisition. Nevertheless, this approach, further popularized by Meunier (2011), became widely used by survey design practitioners because it allows them to compute relative quality (SSE) versus acquisition costs.

With the emergence of high-performance computing (HPC), 3D seismic modeling became an affordable approach to model 3D surveys directly and evaluate the images. Regone et al. (2015) were among the most influential advocates of such a numerical approach. They further made a simplifying assumption that prestack depth migration (PSDM) with an accurate velocity model may be considered a surrogate for complete processing. Yet, their assessment of the resulting images remained subjective and based on human opinions.

While analytical and numerical approaches appear entirely independent, there must be a connection and even agreement between them when applied to the same problem. To our knowledge, however, it was never fully demonstrated. Finally, the modeling-based approach remains costly because 3D elastic modeling coupled with sophisticated model building are compute- and human-intense activities. With most acquisition departments not keeping an HPC expert, geomodeler, and processor (to compare results) on their staff, the numerical approach remains a rare bird. In addition, the economic model for survey cost is much easier optimized using an analytical approach.

In this study, we jointly analyze and combine both approaches in a more powerful way. Specifically, we set to achieve three goals:

This paper is an expansion of Bakulin et al. (2022c), originally presented at the Second International Meeting for Applied Geoscience & Energy.
[1]Saudi Aramco, EXPEC Advanced Research Center, Dhahran, Saudi Arabia. E-mail: andrey.bakulin@aramco.com; ilya.silvestrov@aramco.com.

- harmonize both approaches by attaching an apples-to-apples metric of signal-to-noise ratio (S/N) enabling their direct head-to-head comparison;
- upgrade the numerical approach by coupling it with a data-driven S/N estimation; and
- perform direct validation of the analytical approach using the numerical method with automated data-driven QC on a controlled data set from the elastic SEG Advanced Modeling (SEAM) Arid model.

To our knowledge, such direct modeling-based and data-based validation is being done on a land model with realistic noise for the first time. Surprisingly for some and unsurprisingly for others, most assumptions of the analytical approach were vindicated successfully.

Field and numerical workflows coupled with analytical signal-strength estimate

Among the plethora of approaches for acquisition design, we single out the analytical approach by Meunier and Gillot (2000) as a fundamental method for establishing a feedback loop between acquisition and processing. This approach directly relates the acquisition's input variables to the seismic image's quality. In this study, we limit our discussion to 3D land seismic acquisition with vibroseis sources. Considering that a seismic image results from a combination of migration and stacking processes, Meunier and Gillot (2000) and Meunier (2011) put forward a popular formula for an SSE providing an estimator of S/N of the final seismic image. SSE is derived through the simple square-root combination rule as

$$SSE(f) = Ss(f)\sqrt{SD\,NR\,RA}\,, \tag{1}$$

where RA is the area of the receiver station, NR is the number of receivers per shot point, SD is the source density (number of shot points per surface unit), f is a frequency, and Ss is the source strength. The product of $SD * NR$ is often referred to as trace density (TD), leading to a simpler SSE version:

$$SSE(f) = Ss(f)\sqrt{TD\,RA}. \tag{2}$$

$Ss(f)$ represents source strength defined for vibroseis sources as

$$Ss(f) = Pf\,D\,N_v\sqrt{\tfrac{1}{Sr(f)}}\,, \tag{3}$$

where Pf is the vibrator peak force, D is the drive level, N_v is the number of vibrators in the source array, and $Sr(f)$ is the sweep rate df/dt (Meunier, 2011). It should be noted that SSE can be converted to theoretical S/N in decibels as $SNR^t_{dB} = 20\log_{10}SSE$. Based on a simple assumption of random noise, such a formula is powerful because it allows direct balancing of different trade-offs occurring in seismic acquisition between various parameters at play. It also incorporates the immediate effects of the source/receiver array, allowing us to compare legacy acquisitions with larger groups and newer point-source point-receiver acquisitions.

While acquisition design relies heavily on the SSE equation, it rarely gets to validate the ultimate accuracy of this formula. Processors, seldom familiar with the SSE equation, prefer to use their more complex metrics. As a result, they tend to overestimate the role of the processing, believing that applying their preferred processing technique could overcome many restrictive mundane considerations embedded in SSE. In summary, every processor is biased toward their own qualitative assessment of the final image. Moreover, these assessments might differ significantly among various experts. As a result, the efficacy of different acquisition elements is often subject to vigorous debates, making it hard to reach a broader technical consensus and complicating management decisions.

What if we find a way to directly measure the S/N of the final data volume using a method acceptable to processors and compatible in assumptions with the SSE equation? Likewise, such a method can automate the assessment of synthetic seismic images from the numerical approach (Regone et al., 2015).

We introduce and apply such a method from Bakulin et al. (2022d). They described automated stack-based S/N estimation that works on stacked data and is equally applicable to most challenging prestack data down to −60 dB or less. Armed with such a method, we propose two quantitative workflows for evaluating various acquisition geometries: one for the field (Figure 1a) and another for synthetic data (Figure 1b) for survey design feasibility. The objective of each flow is to quantitatively compare different acquisition geometries with the least possible human intervention and bias. Input to each flow is data acquired or simulated with varying acquisition geometries. Output is human-independent metrics such as

- average S/N of prestack data;
- average S/N of the migrated or imaged data; and
- the difference between the two, ΔS/N, called the imaging budget.

For a numeric workflow with synthetic data (Figure 1b), humans are only left to create the subsurface model. The rest can be fully automated, removing any human bias in assessing the results and hence the survey design process. Following Regone et al. (2015), we assume that migration with a true velocity model is an acceptable proxy for the complete processing sequence on synthetic data. Other simplified approaches (Regone et al., 2015) could be used instead of comprehensive 3D elastic modeling to generate synthetic data for the second workflow (Figure 1b).

Because some legacy data are nearly always available, immediate automated evaluation of prestack S/N allows us to judge if synthetic data have replicated the S/N of legacy field data. If not, then revising the 3D model (or hybrid noise model) is done to achieve the replication. Such a step is crucial for numerical workflow because prestack field data S/N is the most critical factor controlling the success of the imaging project. For example, suppose we simulate a scenario that is too optimistic while field data are noisier. In that case, we likely will select a less dense geometry with an insufficient imaging budget to deliver the expected results. On the other hand, suppose we simulated an overly pessimistic scenario, but real data are simpler. In that case, we achieve the objectives but may have wasted a portion of the acquisition budget.

DOI:10.1190/tle42050310.1

In a field workflow (Figure 1a), we can use conventionally processed data after time or depth processing (less automation) on the field data. However, it becomes more essential to apply consistent processing flows.

Both field and synthetic workflows can now be directly benchmarked against the analytical SSE approach because all methods result in either predicted or measured S/N on the final image. Therefore, closing the loop becomes possible for both field and synthetic flow. We can start answering questions that often remain unaddressed. Did each field or proposed acquisition geometry perform as expected from the SSE formula? If not, what is the likely culprit? Which acquisition parameters needs to be adjusted to reach the target S/N required by final users?

This study presents examples of three typical use cases arising in 3D land seismic practice:

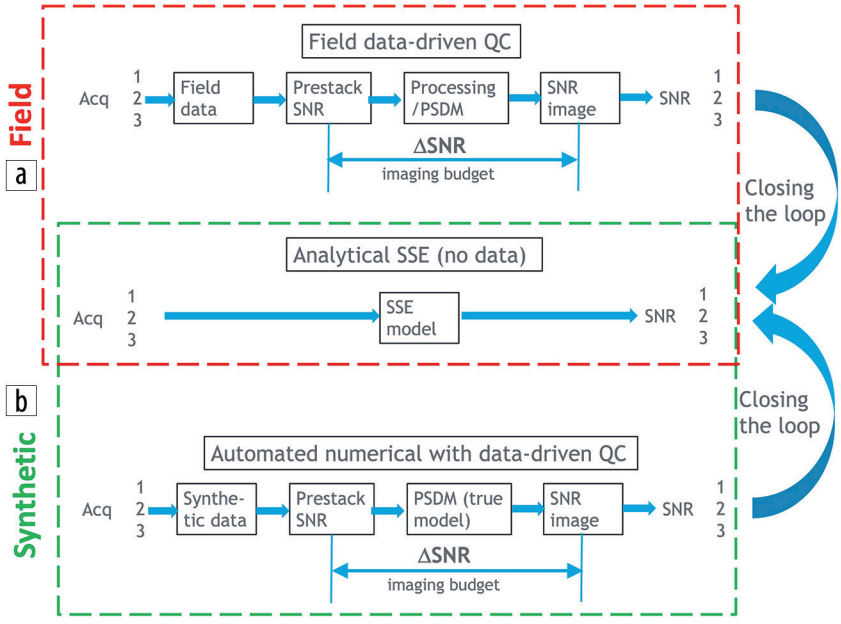

Figure 1. Survey design workflows using (a) field and (b) synthetic data. Both workflows culminate in the S/N (abbreviated here as SNR) of the seismic image for each acquisition geometry. As a result, closing the loop with the analytical SSE approach (middle) enables immediate understanding and analysis.

- quantitatively contrast different 3D data sets acquired with various field acquisition geometries and understand where differences in S/N came from;
- perform a realistic numerical feasibility study evaluating different 3D acquisition geometries with arrays and single sensors and assess their expected performance; and
- predict absolute S/N outcomes of new 3D acquisitions based on the existing legacy data with different acquisition geometry.

These use cases are all based on variations of the field or synthetic workflows from Figure 1. Finally, we discuss lessons learned and speculate on why such exercises can lead to improved survey design practices. Before diving into use cases, let us quickly recount the basics of the S/N estimation method underlying this study.

Data-driven stack-based S/N method

We use a versatile data-driven stack-based S/N method (Bakulin et al., 2022d). Each estimate of S/N requires a 3D data window (two spatial and time directions) consisting of superimposed signal and noise:

$$d_{ij} = s_i + n_{ij}, \quad i = 1, \ldots, N, \quad j = 1, \ldots, M, \tag{4}$$

where $s_i = s(t_i)$ is a signal, $n_{ij} = n(t_i, x_j)$ is noise, i is a time sample, and j is a trace index. Then experimental S/N (SNR^e) is computed by a simple formula using semblance S as an intermediate variable:

$$SNR^e = \frac{S}{1-S}; \; S = \frac{\sum_{i=1}^{N}\left(\sum_{j=1}^{M} d_{ij}\right)^2}{M\sum_{i=1}^{N}\sum_{j=1}^{M} d_{ij}^2}; \; SNR^e_{dB} = 10\log_{10} SNR^e. \tag{5}$$

A moving window runs throughout the 3D data volume, and the computed S/N is output at the center of the window. As a result, the 3D volume of S/N is generated for each input data volume. In the case of imaged data, the two spatial directions are X and Y, whereas the third direction is time or depth. For prestack data, cross-spread, common-depth point, or other gathers are used with two spatial directions and the third direction being time. For both prestack and stack cases, the output is an S/N volume of the same size as an input. Bakulin et al. (2022d) defined the minimum number of traces required for a reliable S/N estimate. Such an ensemble could comprise only tens of traces for imaged data (high S/N). However, it may become tens or even hundreds of thousands of traces for prestack data with very low S/N (Bakulin et al., 2022d).

Field workflow: Assessing different field acquisition geometries

This use case aims to quantitatively contrast two different 3D data sets acquired with various field acquisition geometries and understand where differences in S/N came from. Specifically, we apply the field workflow (Figure 1a) to evaluate the results of two concurrent 3D land acquisitions described by Tsingas et al. (2020). The first acquisition is a conventional high-channel-count (HCC) production survey. In contrast, the second is a distributed source array (DSA) survey with unconstrained blended shooting (Table 1). The blended acquisition allows lowering crossline distances for both shots and receivers from 125 to 75 m without significantly increasing acquisition time. However, blended unconstrained acquisition relies on single vibrators instead of two-vibe arrays used in production surveys.

Our focus here is merely assessing the resulting images and closing the loop with the SSE. Figure 2 shows cross sections from

DOI:10.1190/tle42050310.1

3D time-migrated cubes and associated 3D S/N volumes for each data set. The production survey has generally higher S/N (Figure 2a) in the deeper part. Within the window of interest, the S/N distribution for the blended survey is biased toward lower S/N values compared to the production acquisition (Figure 2e). The average S/N is about 13 dB for a production survey and about 11 dB for a blended survey with DSA (Figure 2f). The difference of about –2 dB (blended minus production) is also confirmed when averaged over the entire 3D volume.

Closing the loop with the SSE formula (Figure 1a) allows an understanding of why this happens. If we ignore minor sweep differences, two significant factors are at play:

- trace density increased by a factor of 2.9 (denser shot and receiver lines); and
- the number of vibrators per source array dropped by a factor of two.

Equations 2 and 3 suggest that $SSE \sim N_v\sqrt{TD}$. The resulting SSE ratio between DSA and production is 0.85, translating into an S/N difference of –1.4 dB (Table 1). As a result, the predicted (–1.4 dB) and measured (–2 dB) average S/N differences are comparable. Closing the loop further allows us to estimate that an additional increase of trace density by a factor of 1.38 is needed for the DSA survey to reach the same S/N as the production survey. DSA-blended point-source shooting enables a much faster acquisition rate. However, an even higher trace density is required to beat the production surveys with two vibrators in a source array. We demonstrate how such trace density could be reliably estimated directly from the field data

Table 1. Comparison of two field acquisition geometries and associated S/N measured on the final image (SNR^e_{dB}) and predicted by the SSE equation (SNR^t_{dB}). Acquisition parameters and data are taken from Tsingas et al. (2020). The middle column is a conventional HCC production survey. The right-hand column is a DSA unconstrained blended survey. Despite a three times increase in trace density, the production survey delivers higher S/N, both measured on the data and predicted by SSE. S/N reduction due to the drop of the two-vibe array overpowers the S/N increase due to higher trace density consistently with the SSE formula.

Acquisition type	Production	DSA unconstrained blended
No. of receiver lines	48	73
No. of channels per line	480	441
No. of active channels	23,040	32,193
Shot point and receiver point distances (m)	25 × 25	25 × 25
Bin size (m)	12.5 × 12.5	12.5 × 12.5
Receiver line distance (m)	125	75
Shot line distance (m)	125	75
Nominal full fold	1808 (@ 6 km offset)	5024 (@ 6 km offset)
Trace density (traces/km^2)	11,000,000	32,000,000
Number of vibes per source array	2	1
Number of geophones per receiver array	9	9
Predicted SNR^t_{dB} (dB)	0 dB (reference)	–1.4
Measured SNR^e_{dB} (dB)	0 dB (reference)	–2

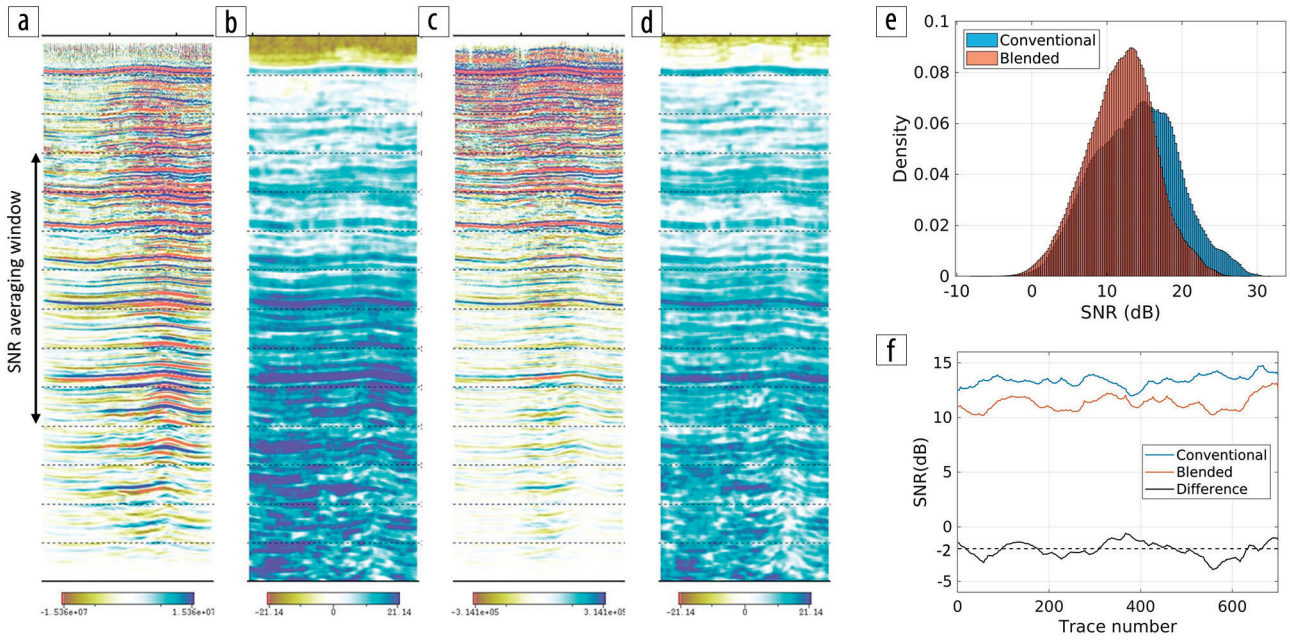

Figure 2. Seismic images and associated S/N panels (in dB) for (a) and (b) the production HCC acquisition and (c) and (d) the blended DSA acquisition. The histograms in (e) show the S/N values' distribution in the vertical time window marked by the arrow. The S/N curves in (f) show averaged values over this window and their difference. The second acquisition has reduced S/N by about –2 dB, which is also evident by visual inspection. The measured S/N difference is consistent with –1.4 dB from the SSE equation, validating its good predictive power.

using the field workflow coupled with the SSE equation (Figure 1a).

Synthetic workflow: Evaluating multiple acquisition geometries using SEAM Arid data set

The second use case performs a realistic numerical feasibility study evaluating different 3D acquisition geometries with arrays and single sensors and assesses their expected performance on a complex SEAM Arid data set representative of a desert environment. Here we apply a second numerical workflow with data-driven QC (Figure 1b) to such elastic synthetic data replicating data quality challenges from arid environments (Oristaglio, 2012; Regone et al., 2017; Bakulin and Silvestrov, 2021; Bakulin et al., 2022c). Figure 3a shows that prestack reflections are overwhelmed by ground roll and other elastic noise. As a result, the average prestack S/N is between –35 and –55 dB (Figures 3b and 3c). The strongest deep reflectors exhibit higher S/N of about –20 dB, for instance, at 1.6 s or 2.5 km depth (Figure 3b). However, most events with a weaker reflectivity exhibit much lower S/N. Note that for reliable estimation of S/N of –40 dB, the ensemble has to contain at least 10,000 traces (Bakulin et al., 2022c).

Let us evaluate six 3D acquisition geometries listed in Table 2 (Bakulin et al., 2022c). For simplicity, we assume the same source strength (3) is used. Geometries G1–G3 resemble HCC data conventionally acquired with nine-geophone arrays in a desert environment (Dmitriev et al., 2017; Tsingas et al., 2020). Geometries G5–G6 represent emerging point-receiver surveys acquired with single sensors. Geometry G4 represents the so-called narrow-azimuth HCC that limits the crossline offset to one-quarter of the inline offset (1.75 versus 7 km). As a result, G4 has shot spacing that is twice as dense in both directions. Although overall trace density (averaged over all offsets) is the same for G4 and G3, narrow-azimuth HCC exhibits variable trace density with offset: it provides a finer sampling of near and mid offsets but compromises the wide-azimuth coverage at far offsets. Figure 4 displays cross sections from full PSDM volumes for all geometries. The first geometry, G1, could not properly image the shallow subsurface (700–2000 m) using conventional processing or true-model PSDM (Bakulin and Silvestrov, 2021). Figure 4 suggests that increasing density could resolve imaging

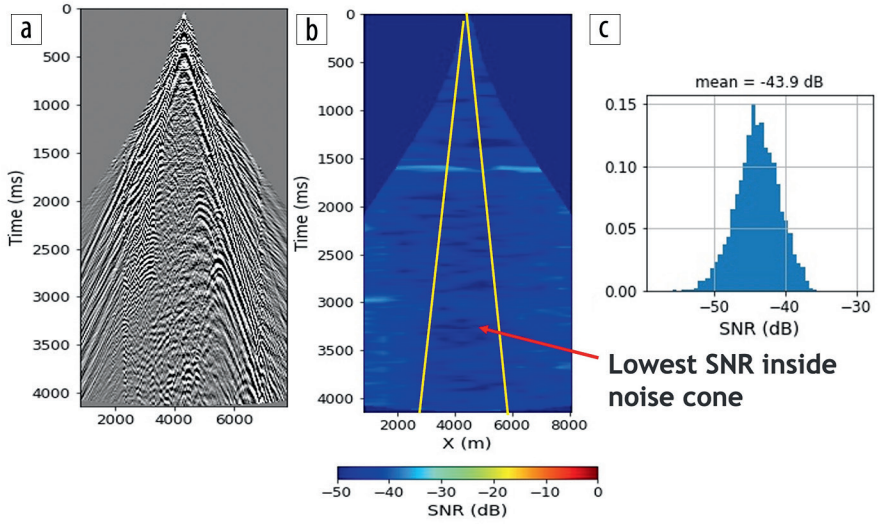

Figure 3. (a) Raw field gather from nine-geophone array data with (b) associated S/N panel and (c) histogram. S/N is estimated using the data-driven stack-based method on 3D ensembles of prestack data.

Table 2. Summary table with evaluated geometries and their theoretical (SNR^t_{dB}) and experimentally measured (SNR^e_{dB}) signal-to-noise ratios. To calibrate predicted and measured dB scales, we assumed $SNR^t_{dB} = SNR^e_{dB}$ for the last geometry G6. HCC denotes high-channel-count geometries with nine-geophone arrays; SS represents single-sensor acquisitions.

Name	Short name	Shot spacing	Receiver spacing	Trace density	SSE	SNR^t_{dB} (shallow)	SNR^e_{dB} (shallow)	SNR^t_{dB} (deep)	SNR^e_{dB} (deep)
Semi-HCC (3 × 3 geophone arrays) (SD = 1, NR = 1, RA = 9)	G1	100 × 50 m	25 × 150 m	1	3	1.5 dB	–1.2 dB	5.7 dB	6.7 dB
HCC (denser, 3 × 3 geophone arrays) (SD = 2, NR = 1.5, RA = 9)	G2	50 × 50 m	25 × 100 m	3	5.2	6.3 dB	1.8 dB	10.5 dB	8.8 dB
Nodal HCC (nodal, 3 × 3 geophone array) (SD = 0.5, NR = 6, RA = 9)	G3	100 × 100 m	25 × 25 m	3	5.2	6.3 dB	3.9 dB	10.5 dB	11.6 dB
NAZ nodal HCC (3 × 3 geophone array) (SD = 2, NR = 1.5, RA = 9)	G4	50 × 50 m	25 × 25 m	3	5.2	6.3 dB	6.4 dB	10.5 dB	11.6 dB
Nodal SS (intermediate) (SD = 2, NR = 6, RA = 1)	G5	50 × 50 m	25 × 25 m	12	3.5	2.8 dB	2.9 dB	7 dB	10.4 dB
Nodal SS (dense) (SD = 2, NR = 24,RA = 1)	G6	50 × 50 m	12.5 × 12.5 m	48	6.9	8.7 dB reference	8.7 dB reference	12.9 dB reference	12.9 dB reference

DOI:10.1190/tle42050310.1

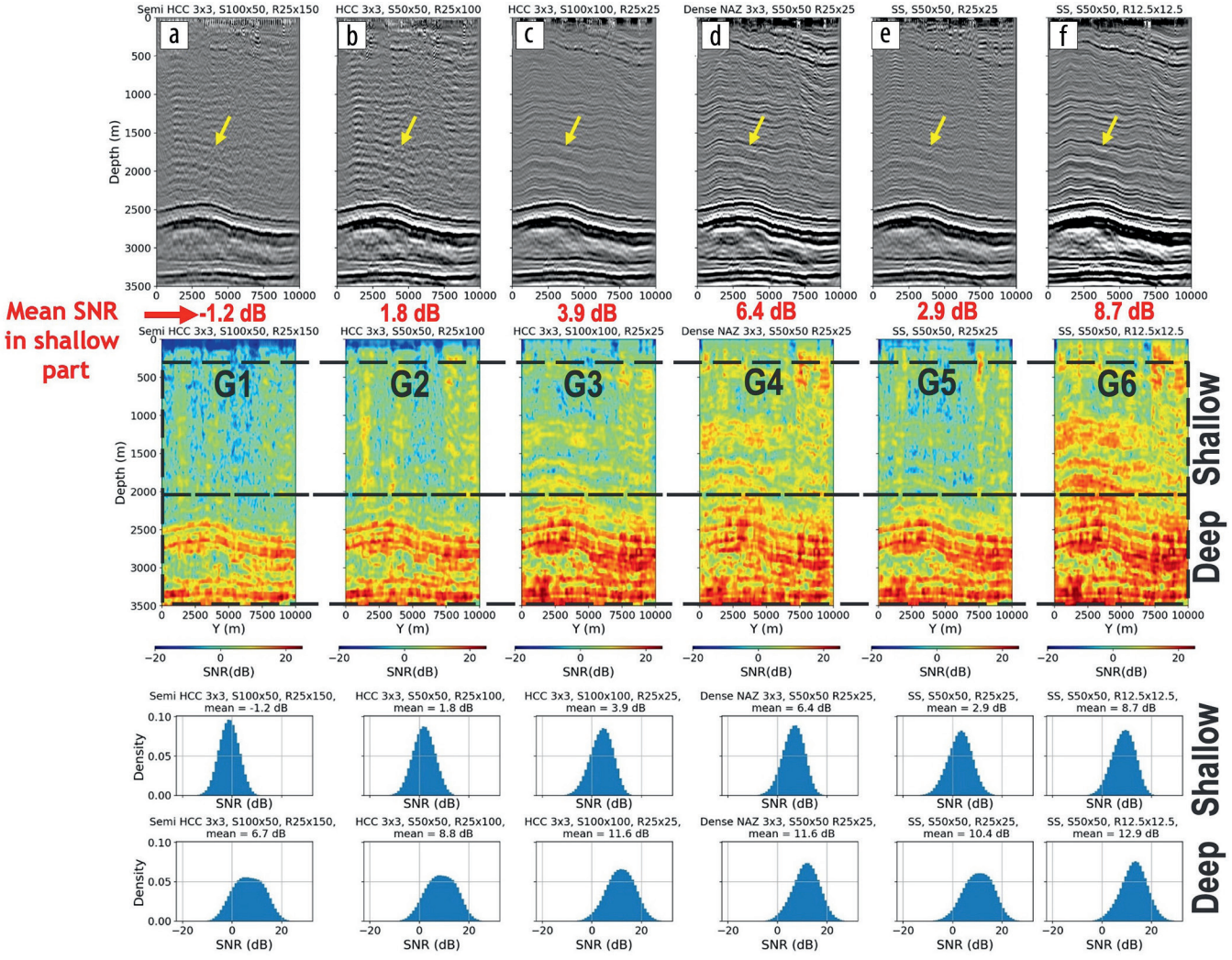

Figure 4. Cross sections from a 3D PSDM volume (top row) and S/N volumes (second row) obtained by migrating raw data with different acquisition geometries: (a) semi-HCC (3 × 3 geophone array) S100 × 50 m, R25 × 150 m; (b) HCC (3 × 3 geophone array) S50 × 50 m, R25 × 100 m; (c) nodal HCC (3 × 3 geophone array) S100 × 100 m, R25 × 25 m; (d) narrow-azimuth HCC (maximum crossline offset is ¼ of inline offset) S50 × 50 m, R25 × 25 m; (e) SS (intermediate) S50 × 50 m, R25 × 25 m; (f) SS (dense) S50 × 50 m, R12.5 × 12.5 m. The two lowest rows show histograms of measured S/N computed over the shallow 700–2000 m (third row) and deeper 2000–3750 m (fourth row) 3D subvolumes. HCC denotes high-channel-count geometries with nine-geophone arrays; SS represents single-sensor acquisitions.

in the shallow part. However, exact progression is nonuniform, and arrays play an essential role. Let us perform a systematic comparison of predicted and measured S/N metrics (Figure 1b) to evaluate the results and, in the process, also validate the usefulness of the analytical SSE model for acquisition design.

S/N volumes. The second row of Figure 4 displays cross sections from S/N volumes. Bakulin et al. (2022d) demonstrated that the stack-based method estimates absolute S/N instead of the SSE equation that only conveys relative S/N. The volumetric representation of S/N is helpful for all kinds of analysis (Bakulin et al., 2022b, 2022c). A simple glance at Figure 4 suggests two different "regimes" of lower S/N in the shallow part (700–2000 m) and higher S/N in the deeper part (2000–3750 m). While shallow and deep reflections may have a similar level of near-surface noise (Figure 3a), the deeper part is characterized by higher reflectivity, increasing S/N values (Bakulin and Silvestrov, 2021). The S/N volume is essentially a calibrated version of the semblance, so coherent events become discernable as stripes of higher S/N. As a result, the numerical value of S/N also carries interpretative significance. To demonstrate that, we compute histograms of S/N distribution for shallow and deeper parts (third and fourth rows in Figure 4). While it is feasible to focus on a target event and associated S/N map, volumetric distributions enable imaging quality assessment in 3D over an extensive vertical depth window. Let us examine the mean value from histograms for a shallow 700–2000 m window (Figure 4, Table 2). The mean value varies from –1.2 dB for G1 to 8.7 dB for G6. A value of approximately 0 dB means that signal and noise are comparable. Measured S/N values (Figures 4a–4d) are consistent with the visual assessment of the actual images with missing (–1.2 dB, Figure 4a), ambiguous (1.8 dB, Figure 4b), or intermittent (3.9 dB, Figure 4c) reflections. A level close to about 6 dB may be a prerequisite for robust structural interpretation. Out of all the volumes, only G4 (6.4 dB) and G6 (8.7 dB) eclipse

that threshold and exhibit crisp boundaries and robustly map channels shown by the yellow arrows.

Comparison of measured and predicted S/N. Let us contrast the predicted and measured S/N values. Because the acquisition formula predicts a single "average" value of S/N (over the entire image and entire frequency band), let us compare them with the mean values extracted from S/N volumes. Table 2 shows such a comparison. The SSE formula predicts relative S/N between different acquisitions. As noted earlier, the average S/N is different between shallow and deep portions, so let us do a separate analysis for the shallow and deep parts. To "calibrate" the predicted and measured S/N scales, let us align them for the densest geometry G6 so that $SNR^t_{dB} = SNR^e_{dB}$. As a result, we may not make any comparison for G6 itself. However, we can now quantitatively relate G6 to the remaining five geometries. For example, going from G6 to G5, shallow S/N drops by 5.8 dB, while prediction also suggests a similar value of 5.9 dB. Crossplotting predicted and measured S/N (Figure 5) demonstrates good agreement between the two sets, both clustering around $SNR^t_{dB} = SNR^e_{dB}$ line with reasonable deviations.

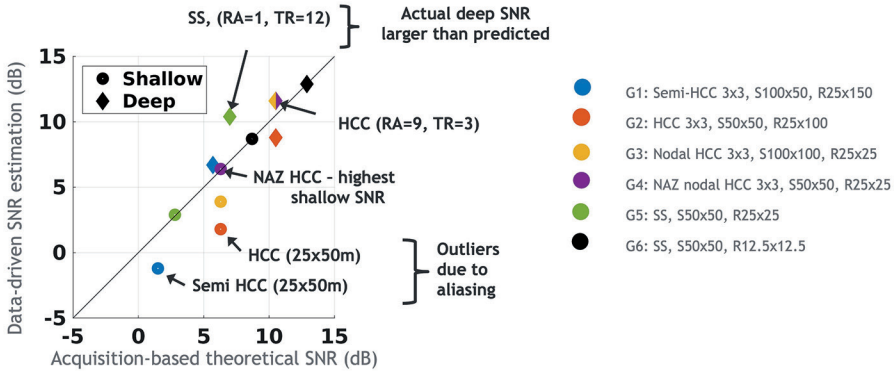

Figure 5. Crossplot of theoretical (SNR^t_{dB}) from SSE and experimentally measured (SNR^e_{dB}) signal-to-noise ratios from Table 2. Observe good agreement between analytical formula and numerical approach with data-driven S/N. The effect of arrays is fully vindicated. HCC denotes high-channel-count geometries with nine-geophone arrays; SS represents single-sensor acquisitions.

More detailed conclusions could be summarized as follows:

1) Acquisition sampling and array size play equally important roles, as predicted by SSE.
2) For successful imaging, two orthogonal directions out of the four acquisition directions must be well sampled (i.e., address aliasing). A similar conclusion was made by Regone et al. (2015). This study suggests that such a threshold sampling for aliasing is 25 m for data with arrays and 12.5 m for single-sensor data in this case.
3) The SSE equation provides a good prediction of observed S/N. However, it fails in the presence of aliasing, suggesting that noise suppression stops following the square-root law. For example, Figure 5 shows that measured S/N for G1 and G2 represent the farthest outliers because only one direction is well sampled in the domain of best sampling in those geometries (25 × 50 m in the cross-spread domain). Also, G2 and G3 have the same SSE. However, when two directions become well sampled in G3 (25 × 25 m), S/N consistently increases by 2.1 and 2.8 dB for shallow and deep (Table 2). Similarly, Regone et al. (2015) observed lessened noise reduction during the migration of aliased data.
4) G4 (narrow-azimuth HCC) exhibits the highest shallow S/N of all three geometries (G2–G4) having the same SSE. We interpret that it provides an extra sampling inside the inner noise cone with the lowest S/N (Figure 3b), thus delivering uplift where needed most (near and mid offsets). Despite concerns that the lack of larger offsets may compromise the deeper part, the average deep S/N of G4 and G3 appear identical. Quantifying variation of S/N with offset (Figure 3) may lead to further optimization of acquisition geometries.

Effect of arrays. The SSE equation 2 suggests that the product of trace density and receiver array size controls S/N. The measured S/N from Table 2 and Figure 4 fully support these conclusions. Suppose we desire single-sensor data of equivalent S/N to a system with arrays. In that case, we must increase trace density by a factor of nine (for nine-geophone arrays considered here). When, instead, trace density is increased by only a factor of four by going from G4 to G5, we observe a drop in measured S/N by 3.5 dB for shallow and 1.2 dB for deep (Table 2). These estimates are comparable with an expected decline of 3.5 dB from the SSE equation. A reduced shallow S/N is visually evident when comparing Figures 4d and 4e. Single-sensor geometry G6, with 16 times the trace density of G4, can finally outperform arrayed HCC data of G4 as manifested by an increase in S/N of 2.3 and 1.3 dB for shallow and deep, respectively (compare Figures 4d and 4f). These values are close to an expected improvement of 2.4 dB from the SSE equation. While the agreements are not perfect, they show good performance of the simple SSE equation on the rather complex realistic synthetic data at hand. The effect of arrays could be more significant for real data due to multiplicative scattering noise (Bakulin et al., 2022a), not included in the simple SSE model above. This perhaps can explain the more significant drop in S/N in real single-sensor data than expected from SSE prediction (Bakulin et al., 2022d).

Imaging budget. Let's take prestack S/N at –44 dB for nine-geophone array data (Figure 3c). The imaging budget estimated from the numerical workflow (Figure 1b) is between 42.7 and 50.2 dB (computed using SNR^e_{dB} for G1–G4 for the shallow part, Table 2). In this case, the imaging budget mainly comes from the advanced migration algorithm. In the case of field data, the budget would also include the effects of various multichannel prestack processing steps. Naturally, the budget is lower for sparser geometries and higher for denser geometries. Nevertheless, this imaging budget number is impressive. Assuming uncorrelated white noise, stacking 10,000 (10^4) traces would increase S/N by 40 dB, whereas stacking 100,000 (10^5) traces improves S/N by 50 dB (Bakulin et al., 2022d). While these trace numbers are

much higher than nominal survey folds, quantifying S/N increases during migration and multichannel processing could enable deeper understanding but requires further studies. Suppose we start routinely measuring the imaging budget in processing. In that case, we accumulate valuable knowledge of what is achievable during typical processing/imaging. Ultimately, we aspire to obtain an analytical SSE-type or empirical model predicting the imaging budget based on the number of traces participating in the final processing and migration.

Field workflow: Predicting absolute S/N outcomes of new acquisitions based on the legacy data

The previous exercises validate that SSE holds predictive power for evaluating land acquisition with arrays and single sensors. They also demonstrate the usefulness of unbiased human-independent data-driven S/N estimation. The third use case predicts absolute S/N outcomes of new 3D acquisitions based on the existing legacy data with different acquisition geometry. It illustrates an example of a quantitative and transparent survey design based on a variation of the field workflow coupled with the SSE equation (Figure 1a). Too often, seismic users are dazzled by fold or trace density numbers that they cannot relate to their desired interpretation products. We aim to translate the survey design into shared S/N language accessible to all users of seismic data.

Table 3 shows the survey design analysis for five different acquisition geometries. The first column (A1) is the existing legacy HCC acquisition with an HCC design using a nine-geophone receiver and two-vibe source arrays. The remaining columns assess four new geometries. Using the SSE equation and assuming legacy acquisition as a reference (0 dB), we can predict the relative performance of four new geometries. They provide a large spread of relative S/N (with respect to the reference) from –7.7 to +7.8 dB. Relative numbers are not as helpful as absolute S/N. Suppose the legacy data quality is already, say, 10 dB. In that case, A2 and A5 are still acceptable alternatives that should result in 11.8 and 8.3 dB, respectively. Without this reference S/N, the outcomes are hard to characterize and debate.

Returning to legacy data and measuring S/N as a calibration or "anchor" point puts us on solid ground. Suppose the actual data-driven S/N of the legacy image is 2 dB (Table 3), which resembles Figure 4b. Then, we can predict the *absolute* S/Ns listed in the last row of Table 3, and our assessment becomes much more definitive. For example, ultra-high-density nodal geometry A5 looks unattractive with close to 0 dB, meaning it may fail to address even structural imaging (similar to Figures 4a and 4b). Note that such a conclusion is impossible based on trace density alone, which is 5.5 higher for A5. Geometry A2 results in 4.8 dB, an incremental improvement from A1, but still potentially struggling to map subtler structural features such as channels (resembles Figure 4c). In contrast, geometry A4 would lead to a significant uplift expected to image all subtle features and produce high-quality amplitude maps (similar to Figure 4f). Generating predicted S/N "calibrated" by legacy acquisition enables quantitative survey design. Interpreters and other users of seismic data do not speak "trace density" language. However, they are fluent in "image S/N language" and thus could start meaningfully contributing to survey design. Quantifying projected absolute S/N could help interpreters decide whether seismic data would suit a specific interpretation task (structural, amplitude, etc.). For example, data volumes with 1–3 dB were deemed unacceptable for robust structural interpretation (Figures 4a and 4b). Data with 3–6 dB may be satisfactory for structure (Figures 4c and 4d), but amplitude maps may not be reliable and require approximately 8–9 dB (Figure 4f) or more (Bakulin et al., 2022b). A similar diagnostic can be applied to prestack data to judge suitability for acoustic impedance inversion and measure S/N progression during processing.

Conclusions

We have presented practical workflows for evaluating the impact of different 3D land acquisition geometries on seismic

Table 3. Predicting absolute S/N of new acquisitions by combining analytical SSE approach and data-driven S/N estimation on legacy surveys. Despite the 5.5 trace density increase, new geometries may provide only either incremental uplift (A2, 1.8 dB) or lead to a substantial decline (A3, –7.7 dB) of S/N if a single vibrator is used in the source array. Calibrating S/N to a data-driven "anchor" S/N from a legacy survey enables quantitative prediction that is meaningful for final users of seismic volume (interpreters, geologists, etc.). Trace density alone does not predict the final quality of the seismic image. HCC denotes high-channel-count geometries with nine-geophone arrays.

Name	A1 (legacy): HCC (2 vibes)	A2: Ultra-high-density HCC (1 vibe)	A3: Ultra-high-density nodal (1 vibe)	A4: Ultra-high-density HCC (2 vibes)	A5: Ultra-high-density nodal (2 vibes)
Geophone array	9	9	1	9	1
Source array (number of vibes per fleet)	2	1	1	2	2
Source spacing (m)	100 × 25 m	25 × 25 m	25 × 25 m	25 × 25 m	25 × 25 m
Receiver spacing (m)	25 × 200 m	25 × 100 m	25 × 100 m	25 × 100 m	25 × 100 m
Trace density (traces/km^2)	11,520,000	64,000,000	64,000,000	64,000,000	64,000,000
Fold	1800	10,000	10,000	10,000	10,000
S/N predicted by SSE (dB)	0.0 reference	1.8	–7.7	7.8	–1.7
Field S/N calibration (dB)	2 (measured on the data)	-	-	-	-
Projected S/N based on HCC legacy data (dB)	2 (measured on the data)	3.8	-5.7	9.8	0.3

DOI:10.1190/tle42050310.1

image quality. We brought analytical, synthetic, and field approaches to a common denominator by invoking equitable data-driven S/N estimation. As a result, it becomes possible to perform head-to-head comparisons and close the loop between synthetic/field data and analytical survey design predictions. Furthermore, using automated data-driven S/N metrics avoids subjective human bias when different processors visually assess various seismic images. We illustrate the application of these new workflows in three typical use cases.

In the first use case, we quantitatively contrast 3D field data sets acquired with two different field acquisition geometries and explain why blended acquisition with tripled trace density resulted in a lower S/N than legacy data. Finally, closing the loop with an analytical approach, we conclude that the reduction of S/N when changing two-vibe arrays to point sources had a more substantial negative impact than the uplift associated with tripling the trace density.

In the second case, we perform a realistic numerical feasibility study evaluating six different 3D acquisitions with arrays and single sensors and assess their expected performance on a complex SEAM Arid data set replicating typical challenges of the desert environment. We showed that the volumetric S/N metric captures observed data quality and eliminates any human bias in the assessment process. We further applied this to close the loop between acquisition and processing. We contrasted measured S/N against predictions from the SSE formula used for survey design. We found overall reasonable agreement between predicted and measured S/N, confirming the usefulness of the SSE model. We emphasize that the synthetic elastic data at hand possess only "geologic near-surface noise" and does not contain any random additive noise as hypothesized by the SSE model. Nevertheless, the reduction of such organized near-surface noise during stacking or migration appears to reasonably follow a theoretical square-root model. Noticeable deviation seems to occur when three acquisition directions remain aliased. However, when two orthogonal acquisition directions out of four become nonaliased, noise reduction seems to follow the SSE equation quite well. This is in agreement with current practices of orthogonal acquisition designs used in the industry. Because the lowest S/N occurs at near-mid offsets, dense narrow-azimuth geometries may provide immediate uplift in addressing this issue. The suggested workflow opens the way to a more automated feasibility study of different acquisition geometries based on data-driven S/N estimation on depth-migrated volumes. In addition, the numeric approach with data-driven QC allows for tackling more complex phenomena, such as multiplicative noise caused by small-scale near-surface scattering, which plays a big role in the field data but is not significant in the SEAM Arid model at hand. We expect such multiplicative noise causes significant additional complexity, which explains why single-sensor data from the desert environment are significantly more challenging than expected.

The third use case predicts absolute S/N outcomes for four new 3D acquisitions with arrays and single sensors based on the existing legacy data with different acquisition geometry. Using legacy data S/N as a calibration point, we can predict the expected absolute S/N that could be discussed directly with the ultimate users of seismic volumes who may not speak the trace density language adopted by acquisition specialists. Such transparent and quantitative survey design improves communication between geoscientists and enables more effective decision-making. TLE

Acknowledgments

We thank Maxim Protasov (Institute of Petroleum Geology and Geophysics) for his assistance in developing and implementing the stack-based S/N method, Pierre Leger (former Saudi Aramco) for processing volumes with various geometries, and Mohammed Mubarak (Saudi Aramco) for assistance with the DSA data.

Data and materials availability

Data associated with this research are confidential and cannot be released.

Corresponding author: ilya.silvestrov@aramco.com

References

Bakulin, A., and I. Silvestrov, 2021, Understanding acquisition and processing challenges in the desert environment through SEAM Arid and Barrett models: First International Meeting for Applied Geoscience & Energy, SEG/AAPG, Expanded Abstracts, 2824–2829, https://doi.org/10.1190/segam2021-3583002.1.

Bakulin, A., D. Neklyudov, and I. Silvestrov, 2022a, Multiplicative random seismic noise caused by small-scale near-surface scattering and its transformation during stacking: Geophysics, **87**, no. 5, V419–V435, https://doi.org/10.1190/geo2021-0830.1.

Bakulin, A., M. Protasov, and I. Silvestrov, 2022b, Robust post-stack and prestack signal-to-noise ratio estimation on land seismic data: 83rd Conference and Exhibition, EAGE, Extended Abstracts, https://doi.org/10.3997/2214-4609.202210099.

Bakulin, A., I. Silvestrov, and P. Leger, 2022c, Closing the loop between acquisition and processing: Data-driven volumetric SNR estimation versus acquisition design predictions: Second International Meeting for Applied Geoscience & Energy, SEG/AAPG, Expanded Abstracts, 46–50, https://doi.org/10.1190/image2022-3735804.1.

Bakulin, A., I. Silvestrov, and M. Protasov, 2022d, Signal-to-noise ratio computation for challenging land single-sensor seismic data: Geophysical Prospecting, **70**, no. 3, 629–638, https://doi.org/10.1111/1365-2478.13178.

Dmitriev, M., A. Bakulin, and P. Golikov, 2017, Efficient four-dimensional supergrouping algorithm for enhancement of high-channel count seismic data: 87th Annual International Meeting, SEG, Expanded Abstracts, 4986–4990, https://doi.org/10.1190/segam2017-17668141.1.

Galbraith, M., 2000, 3D seismic survey design: A solution: First Break, **36**, no. 12, 171–176.

Hornman, K., and G. Vermeer, 2000a, Introduction to 3D design problem: First Break, **36**, no. 12, 161.

Hornman, K., and G. Vermeer, 2000b, Overview of solutions: First Break, **36**, no. 12, 184–185.

Lansley, M., 2000, 3D seismic survey design: A solution: First Break, **36**, no. 12, 162–166.

Meunier, J., 2011, Seismic acquisition from yesterday to tomorrow: SEG/EAGE, Distinguished Instructor Series, no. 14, https://doi.org/10.1190/1.9781560802853.

Meunier, J., and E. Gillot, 2000, 3D seismic survey design: A solution: First Break, **36**, no. 12, 176–179.

Monk, D., and M. Yates, 2000, 3D seismic survey design: A solution: First Break, **36**, no. 12, 180–183.

Musser, J., 2000, 3D seismic survey design: A solution: First Break, **36**, no. 12, 166–171.

Oristaglio, M., 2012, SEAM Phase II — Land Seismic Challenges: The Leading Edge, **31**, no. 3, 264–266, https://doi.org/10.1190/1.3694893.

Regone, C., M. Fry, and J. Etgen, 2015, Dense sources vs. dense receivers in the presence of coherent noise: A land modeling study: 85th Annual International Meeting, SEG, Expanded Abstracts, 12–16, https://doi.org/10.1190/segam2015-5833924.1.

Regone, C., J. Stefani, P. Wang, C. Gerea, G. Gonzalez, and M. Oristaglio, 2017, Geologic model building in SEAM Phase II — Land seismic challenges: The Leading Edge, **36**, no. 9, 738–749, https://doi.org/10.1190/tle36090738.1.

Tsingas, C., M. S. Almubarak, W. Jeong, A. Al Shuhail, and Z. Trzesniowski, 2020, 3D distributed and dispersed source array acquisition and data processing: The Leading Edge, **39**, no. 6, 392–400, https://doi.org/10.1190/tle39060392.1.

Vermeer, G., 2012, 3D seismic survey design, 2nd edition: SEG, https://doi.org/10.1190/1.9781560803041.